Quantitative Analysis of Reaction Front Geometry in Detonations

F. Pintgen, and J.E. Shepherd
Graduate Aeronautical Laboratories
California Institute of Technology
Pasadena, California 91125

Abstract

We present a quantitative analysis of the OH front geometries obtained with Planar Laser Induced Fluorescence (PLIF) imaging in detonations in Ar and N_2-diluted mixtures of H_2-O_2 and H_2-N_2O. A total of 70 PLIF images have been analyzed to determine the degree of complexity for mixtures of different cellular regularity. The geometric complexity is characterized both in terms of the effective reaction front length and an effective dimensionality. As part of this analysis, we have determined the resolution of the optical system and the effective range of scales that can be measured with this technique. The degree of geometric complexity was found to correlate well with the effective reduced activation energy, which, in turn, is a measure of the degree of cellular regularity. The significance of the smallest observed scales is discussed in relation to the possible relevance of diffusive transport to mixing and combustion within the reaction zone.

Introduction

Previous observations (Pintgen et al., 2003b, Pintgen, 2000) on the reaction zone structure of propagating detonations show that mixtures with very regular cellular patterns have smooth reaction fronts as visualized by Planar Laser Induced Fluorescence (PLIF) images of the OH radical. Mixtures with more irregular cellular structure exhibit (Pintgen et al., 2003a, Austin, 2003) shear flow instabilities and fine scale wrinkling of the reaction front. From the PLIF and schlieren images, the reaction front appears to be geometrically complex in the case of irregular cellular structure. The extent of geometric complexity is an important issue (Singh et al., 2003) in determining the relative roles of chemical reaction associated with shock compression as compared to diffusive transport.

In the present paper, we carry out quantitative analysis of the reaction front geometry complexity by analyzing PLIF images and the imaging system. The reaction front geometry is characterized by examining two characteristics: the rectified length and the effective dimension. The geometric and the stability characteristics of the mixtures are correlated using, as a figure of merit, the reduced effective activation energy as computed from detailed chemical reaction mechanisms. The mixtures studied vary in the degree of cellular regularity from "regular" to "highly irregular", corresponding to reduced activation energies θ between 5.2 and 12.4.

Experimental Setup

The experiments were carried out in an 8 m long detonation tube attached to a 150 × 150 mm square test section, described in more detail in Pintgen (2000). The detonation velocities are obtained from six pressure transducers, three of which are in the test section, and are within 5% of the calculated Chapman-Jouguet (CJ) value. PLIF employing the OH radical is used to visualize the reaction front through a 150 mm diameter quartz window in the side wall of the test section.

An excimer pumped tunable dye laser (Scanmate2E, Lambda Physik) with a frequency doubling unit delivers a pulse of narrow bandwidth UV light with a pulse duration of 20 ns and pulse energy of approximately 6.5 mJ. The frequency was tuned to 284.008 nm which corresponds to the immediate vicinity of two OH transitions: $A^2\Sigma^+ \leftarrow X^2\Pi_i(1,0)$ $Q_2(8)$ and $A^2\Sigma^+ \leftarrow X^2\Pi_i(1,0)$ $Q_1(9)$.

A light sheet was formed by a combination of a cylindrical lens (focal length -25 mm) and a spherical lens (focal length 1000 mm) and enters the test section through a quartz window in the test section end plate. The induced fluorescence, filtered by a bandpass filter (centerline 313 nm, FWHM 10 nm), is collected perpendicular to the light sheet by a 576 × 384 pixel 12-bit intensified CCD-Camera (Princeton Instruments ITE/ICCD-576, 22 × 22 μm pixel size), which was gated by a 90 ns pulse of 900 V. The image is formed by a 105 mm f/4.5 UV-transmitting lens (Nikon UV-Nikkor). The height of the imaged region was between 30 and 75 mm depending on the particular experiment.

Characterization of Mixtures

Stoichiometric H_2-O_2 and H_2-N_2O mixtures diluted with Ar or N_2 at initial conditions of 20 kPa and 20°C were investigated and images from a total of 70 shots were analyzed. One PLIF image is obtained from each experiment. The distinct fluorescence front seen in all PLIF images indicates the location of the sharp rise in the OH concentration at the end of the induction zone as discussed by Pintgen (2004). The exponential rise in OH concentration coincides approximately with the sharpest temperature increase as seen in the calculated OH profiles of Fig. 1. In the present study, we will refer to the leading edge of the OH front simply as the "reaction front".

The induction zone length of the mixtures was calculated with the one-dimensional ZND model (Shepherd, 1986) together with the validated detailed chemical kinetics mechanism of Mueller et al. (2000) and the gas phase chemistry library of Kee et al. (1989). The distance between the leading shockwave and the sharpest increase in OH concentration is within 3% of the distance to the steepest temperature increase for all mixtures. The reaction zone length at CJ conditions for the mixtures studied varies from 0.8 to 7.5 mm (Table 1). The cell sizes ranged from 22 to 110 mm as measured with soot foils placed on the side wall of the test section. It was difficult to assign a cell size S for the marginal mixtures, $S \geq 80$ mm, or when a large range of cell sizes was present. For these cases, the largest cell size observed on the soot foils is given.

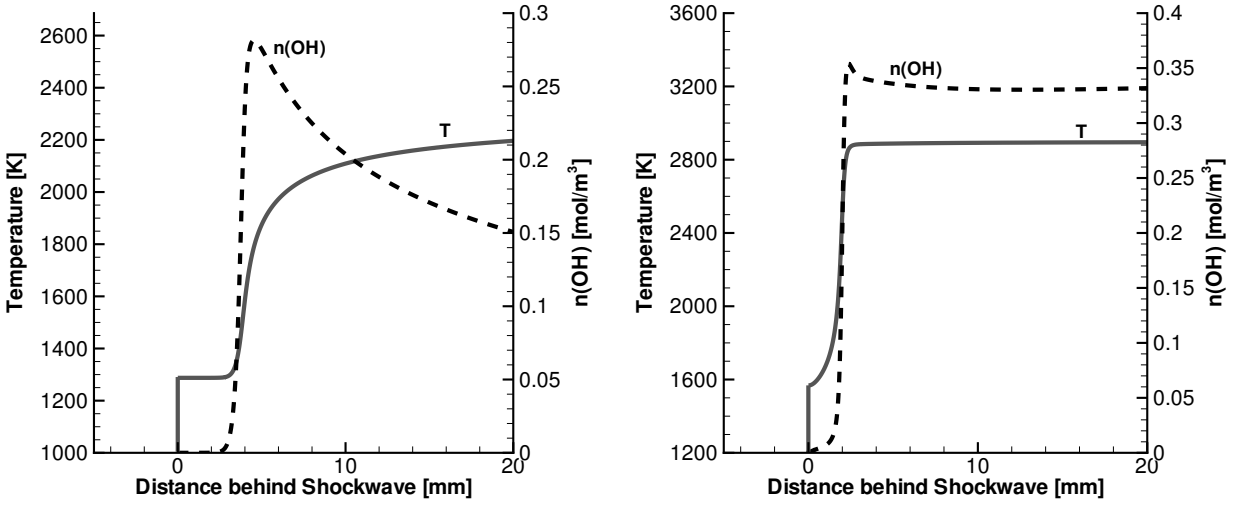

Figure 1: ZND profiles of temperature and OH number density for CJ detonation in (a) $18H_2$+$9O_2$+$73N_2$, P_0 = 320kPa, θ = 7.9, (b) $25H_2$+$25N_2O$+$50N_2$, P_0 = 30 kPa, θ = 11.5.

The reduced activation energy θ was calculated by numerically evaluating the derivative of the induction time t_i with respect to the post-shock temperature

$$\theta = \left(\frac{T}{t_i} \frac{dt_i}{dT} \right)_{vN} . \tag{1}$$

The differentiation was carried out using a temperature perturbation of 1% in a constant volume explosion computation with initial conditions given by the post-shock (vN) state and the same detailed chemical reaction mechanisms used for the ZND model. Considering the process as being modeled by a one-step reaction with an activation energy

Mixture	θ	$(dT/dx)_{max}$ [mm]	$(dn(\mathrm{OH})/dx)_{max}$ [mm]	S [mm]
$13.3H_2$+$6.6O_2$+80Ar	5.2	0.7	0.68	22
$10H_2$+$5O_2$+85Ar	5.6	1.4	1.3	46
$15.3H_2$+$7.6O_2$+$67N_2$	6.8	2.2	2.1	73
$18H_2$+$9O_2$+$73N_2$	7.9	3.9	3.8	104
$16.6H_2$+$8.3O_2$+$75N_2$	8.8	6.2	6	not measured
$25H_2$+$25N_2O$+$50N_2$	11.5	2.9	2.9	54
$20H_2$+$20N_2O$+$60N_2$	12.4	7.4	7.6	110

Table 1: Reduced activation energy, reaction zone length based on the maximum temperature and OH number density gradient, and cell size.

E_a, we can show that $\theta = E_a/RT_{vN}$, which is one of the key parameters controlling the instability of detonations to perturbations and, by extension, the nonlinear evolution of highly unstable propagating waves. For the $2H_2$-O_2-βAr mixtures, θ varies from 5.2 to 5.6 ($\beta = 12$ to 17) and, for the most irregular mixtures of H_2-N_2O-βN_2, θ reaches values up to 12.4 for $\beta = 3$. Intermediate values of θ were found for the N_2-diluted mixtures of H_2-N_2O and H_2-O_2.

The usual subjective interpretation of the degree of regularity observed on soot foils, classified as "regular", "irregular", and "highly irregular", correlates well (Pintgen et al., 2003a) with the magnitude of θ. Mixtures with higher values of θ exhibit an irregular cellular pattern on soot foils. The H_2-O_2-Ar mixture represents a mixture with a very regular cellular structure. The N_2-diluted H_2-O_2 mixture is an example of a more irregular mixture, whereas the H_2-N_2O mixture diluted with N_2 is a highly irregular mixture. Cellular substructure has been observed previously (Libouton et al., 1981) in the H_2-N_2O system. The irregularity and substructure seems to be a general feature of mixtures with high activation energy and has been shown (Austin, 2003) to also apply to hydrocarbon fuels.

Analysis of the Imaging System

It is obvious from visual examination of the PLIF images that the reaction fronts of mixtures classified as "irregular" have a much greater geometric complexity than those of the "regular" mixtures. However, to go beyond this simple observation and make a quantitative analysis of the reaction front geometry requires an evaluation of the imaging system qualities. The key issues of motion blur, modulation transfer function, light sheet thickness, and image processing are discussed in this section.

The PLIF imaging system is operating in the quenching-dominated regime, and the characteristic lifetimes of OH radicals in the excited state are significantly shorter than the laser light pulse of 20 ns. Therefore, the induced fluorescence occurs within the duration of the laser pulse. The longer camera gate width of 90 ns is needed because of the laser jitter of 50 ns. The motion blur induced by the length of the laser light pulse was estimated to be approximately 40 μm at CJ conditions, which corresponds to 0.5 pixel for an image height of 45 mm.

For an ideal imaging system, the image height of 30 to 75 mm corresponds to a nominal resolution of 50 to 130 μm/pixel. Due to aberrations occurring for the low f-number optics and the non-ideal modulation transfer function (MTF) of the ICCD-assembly, the point spread function (PSF) is known (Clemens, 2002) to have a broader profile than the diffraction limited blur spot diameter. In the present study, the f-number was 4.5 for all images. The blur spot diameter was calculated to be 7 μm for an image height of 45 mm.

The line spread function (LSF), the one-dimensional analog to the PSF, was determined by imaging a knife-edge moving across the object plane in steps of 10 μm in front of back-illuminated frosted glass as described in Clemens (2002). The image height was

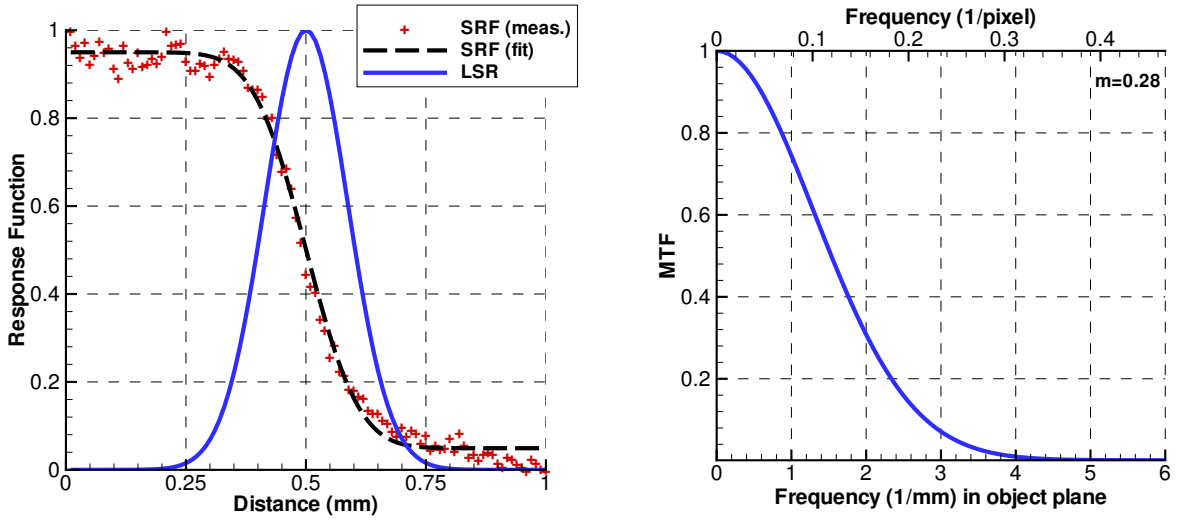

(a) (b)

Figure 2: (a) Measured SRF and from the error function curve fit derived LSF for the camera system used; object height: 45 mm. (b) Modulation transfer function inferred from the LSF

45 mm, which corresponds to a magnification m of 0.28. Since the MTF depends on m, we used the same setup as in the experiments except for the gate width, which had to be set to 3 ms in order to use the full dynamic range just as in the experiment. The spectral line filter was placed in front of the lens as in the experiment. The step response function (SRF), where LSF(x)=dSRF$(x)/dx$, was averaged over ten images and is shown in Fig. 2. The LSF has a $1/e^2$ full width of 350 μm, which corresponds to 5 pixel at this magnification. The MTF is the Fourier transform of the LSF and measures the contrast transfer as a function of the spatial frequency of the irradiance. For our MTF, sine wave structures with a wavelength of 0.5 mm in the object plane, corresponding to a frequency of 2 mm^{-1}, will be imaged with only 30% of their original contrast (Fig. 2). For the signal-to-noise ratio observed in the majority of the images, the cut-off frequency for a minimum visibility corresponding to a contrast ratio of 10% was estimated to be approximately 4.5 pixel.

The images were low-pass filtered before being down-sampled to half the resolution with bi-cubic interpolation. The down-sampling was necessary to allow for an edge detection. The images were then edge-detected with a second-order edge detector (Laplacian of Gaussian, σ=2, filter size: 13×13 pixel), and the threshold for the Laplacian was set manually for each image. Due to fluorescence intensity fluctuations caused by the non-uniform light sheet intensity over the image height, each image had to be processed individually. The smallest feature size resolved with this technique was 6-7 pixel based on the original image size as determined by processing test images like the Koch curve. The test images were degraded with the MTF and processed in the same fashion as the

actual images. For an image height of 45 mm (m=0.28), this resolution corresponds to 410 μm in the object plane (Fig. 3).

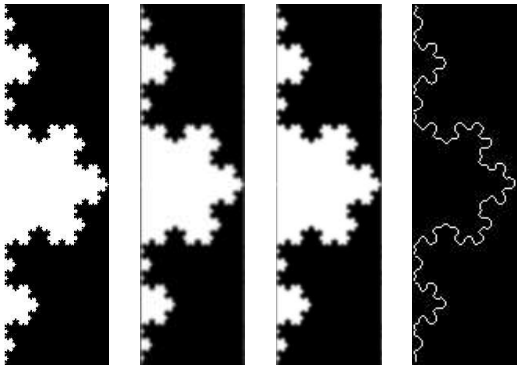

Figure 3: Effect of imaging system on a model complex boundary consisting of the Koch curve. a) Initial test image b) filtered by measured MTF of imaging system. c) down-sampled d) edge-detected.

The light sheet thickness at the focal point was estimated to be 140 μm FWHM by measuring the spatial profile of the laser output beam and assuming ideal focusing optics. For a Gaussian profile of the beam, 75% of the energy is within that thickness. Test-burns on thermal paper indicate a larger thickness of 300 μm, which might be caused by the sensitivity of the thermal paper, which makes it difficult to resolve the full range of the irradiance. For $m = 0.28$, the light sheet thickness corresponds to 2 and 4.5 pixels, based on ideal beam propagation and thermal paper burns, respectively. The distance over which the beam diameter does not exceed 1.4 times the value at the beam waist was estimated to be 15 cm, and, therefore, the change in light sheet thickness in the region of interest can be considered as small.

The conclusion from considering all of these effects is that the resolution is not limited by the digital nature of the ICCD but rather by the illumination technique and the degradation of the image due to the contrast reduction resulting from the other optical components, the lens and intensifier. The smallest scale resolvable depends on the image height (Table 2) and for images between 30 to 70 mm high ranges from 0.5 to 1 mm. This estimate is based on summing the separate influences of the MTF, light sheet thickness, and motion blur. The MTF was measured only for $m = 0.28$ and approximated as constant for the range of magnifications used. The resolution is given in terms of actual physical dimensions of the object. Comparing the values in Tables 1 and 2, we see that we can resolve features that are, in the best cases, one order of magnitude smaller than the ZND-CJ reaction zone length and two orders of magnitude smaller than the cell size. In the worst cases, the resolution is comparable with the ZND-CJ reaction zone length. Fortuitously, the resolution is best for the irregular cases where we are most interested in resolving the largest range of scales possible.

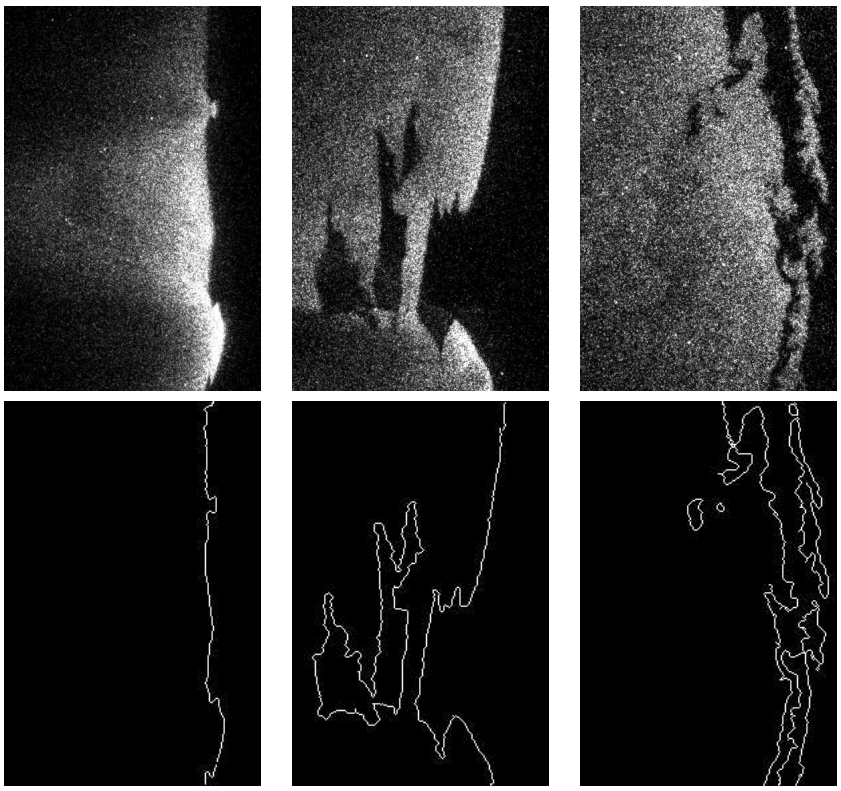

a) $\theta = 5.6$ b) $\theta = 7.8$ c) $\theta = 12.4$

Figure 4: Three examples of original PLIF and edge-detected images. a) Shot 1653, $2H_2$+O_2+17Ar, image height: 40 mm, cell size: 47 mm; b) Shot 1619, $2H_2$+O_2+$6N_2$, image height: 30 mm, largest cell size observed on soot foil 80 mm; c) Shot 1591, H_2+N_2O+$3N_2$, image height 30 mm, largest cell size observed on soot foil: 120 mm

Normalized Reaction Front Length

Three examples of edge-detected images for $\theta = 5.3$, 7.8, and 12.4 are shown in Fig. 4. One measure of complexity is the total edge length normalized by the image height. The minimum normalized edge length l is $l = 1$ by construction. Note that isolated regions of reacting and unreacting fluid contribute to the total edge length. The edge is, in some

image height (mm)	30	45	70
magnification m	0.42	0.28	0.18
MTF and edge detection (mm)	0.36	0.54	0.85
light sheet and motion blur (mm)	0.18	0.18	0.18
smallest scale total resolvable (mm)	0.54	0.72	1.03

Table 2: Overview of the smallest scale resolvable for various image heights considering the effects of the MTF, the edge detection process, motion blur, and light sheet thickness.

cases, not a continuous line, but is made up of several segments (Fig. 4b and c) which are either closed (islands or lakes) or beginning and ending at the image edge. The total edge length is calculated by piecewise-linear approximations, counting all 4-connected pixel pairs of the edge as length 1 pixel and diagonally connected pixel pairs as length $\sqrt{2}$ pixel.

Results

The normalized edge lengths measured for the "regular" mixtures (Ar-diluted H_2-O_2) range from the minimum of 1 up to 1.8, small compared to the other mixtures studied (Fig. 5). For higher reduced activation energies θ, the maximum normalized edge length increases and, for mixtures with $\theta \approx 8$, reaches values up to 4.2. The minimum normalized edge length appears independent of θ and close to 1. For the "highly irregular" mixtures ($\theta = 12.4$), values of normalized edge length up to 7.5 are measured. The current analysis does not allow for a comprehensive statistical characterization, but clearly shows the increasing complexity of the reaction front with increasing θ.

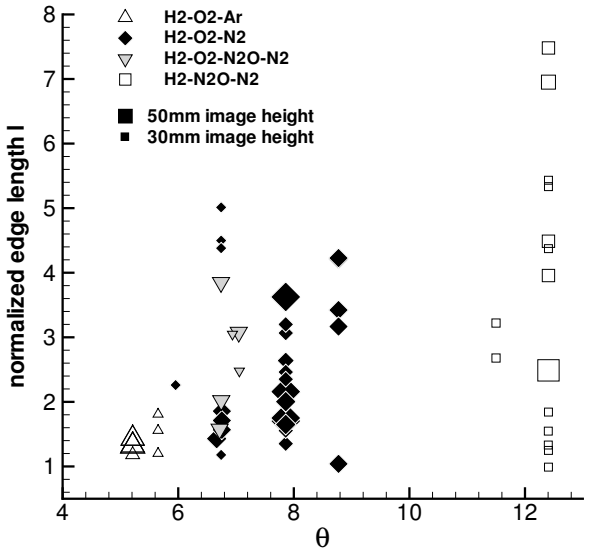

Figure 5: Normalized edge length as a function of the reduced activation energy θ. Symbol size scales with height of field of view.

Discussion

The key limitation of this and all other techniques based on light sheet illumination is the lack of out-of-plane information. Due to the high-speed nature of flow and the apparatus we are using, we are also unable to obtain more that one realization per experiment. Based on our experience (Pintgen et al., 2003b) with more regular mixtures, we can

identify several effects these limitations can mask and potential misconceptions when interpreting these images.

One of the most significant issues is that three-dimensional effects caused by the orientation of the cellular structure to the light sheet can produce artificially long reaction zones. This is due to the random orientation of the cellular structure with respect to the light sheet causing separated islands of higher and lower fluorescence regions. This partially accounts for the large range of normalized edge lengths measured. The image height and cell size influence the probability of three-dimensional effects on the images. The number of shots analyzed for one specific mixture is too small to make a statement about the correlation between normalized edge length and image height. For the mixture $2H_2+O_2+8.1N_2$, $\theta = 7.8$, 14 shots have been analyzed with image heights 40, 50 and 57 mm, and no clear trend can be seen for edge length dependence on image height.

Another effect occurs if the image height is smaller than the cell size. Due to the seemingly random variations in the phasing of the transverse waves, the field of view can correspond to different arrangements of the transverse waves and phases of the cellular cycle. The phase close to the end of a cellular cycle is known to exhibit, for more regular mixtures a large-scale keystone-shaped region of lower fluorescence, which leads to a much larger edge length. In contrast, if the region in the middle of the cell cycle is captured, the reaction front is known to be smooth for Ar-diluted H_2-O_2 mixtures and the normalized edge length is close to its minimum value of one. These effects also contribute to the large range of observed edge lengths.

Despite these issues in interpretation, it is clear from inspecting Fig. 5 that the effective reaction front transverse length is one order of magnitude larger for irregular mixtures than for the regular mixtures. The origin of this lengthening and the significance for detonation front propagation mechanisms is discussed in the Conclusions.

Box Counting Analysis on the Reaction Front

In a second approach to quantitatively describing the geometry of the reaction front, analysis commonly used (for example, see Catrakis and Dimotakis, 1996) for fractal-like objects was conducted on the edge-detected images. The edge-detected reaction front describes a convoluted curve with a scale-dependent length. Note that we do not claim that the edge-detected OH PLIF images are fractals, but simply are using techniques from the fractal analysis to describe quantitatively the geometric complexity. The discussion here is limited to curves with a topological dimension of one and embedding dimension of two. A variety of methods, all based on multiple resolution analysis, is used to determine the dimension D of empirical curves. The key idea is to use the functional dependence of the curve length L on the scale λ to define D. The most common approaches are the yard stick and box-coverage method, which will be applied here. The coverage length L is defined in terms of the box-coverage count $N(\lambda)$, the number of non-overlapping boxes

needed to cover the curve, and the box size λ, defined as the square-root of the box area.

$$L(\lambda) = \lambda\, N(\lambda) \tag{2}$$

$$D(\lambda) = -\frac{\mathrm{d}\log N(\lambda)}{\mathrm{d}\log \lambda} \tag{3}$$

By plotting $\log N(\lambda)$ versus $\log \lambda$, the dimension D can be visualized as the negative slope of this graph. If the slope is not constant, then the curve may be referred to as a scale-dependent fractal for which the dimension depends on the scale λ. The minimum dimension is the topological dimension 1, which corresponds to a straight line. For empirical fractals, a power law dependence typically occurs over a range of scales $\varepsilon_i \leq \lambda \leq \varepsilon_o$, where ε_i and ε_o are the inner and outer cut-off, respectively. In the case of the PLIF images, the fractal analysis can be applied over only a limited range of scales, bounded on the upper side by the field of view, and on the lower side by the resolution of the optical system.

Two sets of box (tile) sizes were used. One set was picked such that the image could be covered for every tile size in an integer number of tiles, which resulted in tiles of size 2×2, 4×4, 8×8, 16×16, 32×32, 96×96, and 288×192, the size of the down-sampled image. The other set was chosen with dimensions $2^n \times 2^n$ with n = 0,1,2,..,8, which describes even horizontal and vertical subdivision of each tile in successive steps. When using the latter set of tile sizes, in some cases only fractions of tiles were covering the image. This leads to coverage lengths $L(\lambda)$ which over-predict the true length, since some tiles extend outside the image. Due to the limitations of non-integer tiling, data from only the first tile set are presented here.

Another effect, most simply illustrated with an example, arises from dividing the tile size by two in the horizontal and three in the vertical direction when changing the tile size from 288×192 to 96×96. Assume a straight vertical line in the right half of the image. For the tile size 288×192, $N = 1$ and $\lambda = L = 235$ and, for the tile size 96×96, $N = 3$, $\lambda = 96$, and $L = 3\lambda = 288$, which shows the unwanted effect of increasing coverage length for a one-dimensional object. To avoid this effect, the largest tile size was set to 288×288, so that all tiles are square.

Results

Coverage counts N for six representative PLIF images, including the ones from Fig. 4, are shown in Fig. 6a as a function of the normalized tile size λ/λ_0, where λ_0 is the largest tile size used. The coverage count is a monotonically increasing function with decreasing tile size and the slope is slightly decreasing with decreasing λ. The H_2-O_2-Ar mixtures have the lowest slope, close to one, which indicates the least complexity in reaction front geometry. The trends for the coverage length (Fig. 6b) are consistent with our intuitive evaluation of the images and the range of total edge lengths shown in Fig. 5.

The coverage length is almost independent of the tile size for the two lower activation energy mixtures and $L_{max}/\lambda_0 < 1.25$, indicating that these fronts are very smooth and

made up of only a few line segments. For the higher activation energy cases, the normalized coverage length L/λ_0 increases rapidly with decreasing λ/λ_0. The coverage length appears to reach a limiting value at the values of $\log_{10}(\lambda/\lambda_0) \leq -1.6$ corresponding to tiles smaller than approximately 8×8 pixel, which is a 1.25 mm object height for an image height of 45 mm. The limiting value of L/λ_0 is an increasing function of the reduced activation energy. For $\theta = 12.4$, the limiting value of $L/\lambda_0 = 5.6$, which is consistent with the maximum value of 7.5 from Fig. 5. The limiting value for L/λ_0 is, in part, caused by the continuously decreasing contrast ratio for higher spatial frequencies.

The dimension (Fig. 7) was found for each image using a linear least-squares fit to determine D in the relationship

$$\log(N) = -D \log(\lambda/\lambda_0) + constant \tag{4}$$

for the range -1.9 $\leq \log(\lambda/\lambda_0) \leq$ -0.5, corresponding to tile sizes from 4×4 to 96×96. The choice of the inner cut-off for this fit is motivated by the previous considerations involving the MTF of the imaging system resolution. The inner cut-off corresponds to the smallest feature size that can be visualized according to our analysis of the imaging system. The upper bound was taken to be one size smaller than the 288×288 tile, which is larger than the image. The cut-off scales are somewhat arbitrary but similar results for the dimension were obtained by changing the cut-off scales by one tile size up or down.

Similar to the normalized edge length, a range of dimensions is obtained for each θ. For $\theta \leq 6$, the spread is small and the dimensions range from 1.05 up to 1.15. For intermediate values of θ, the dimensions range between 1.05 and 1.4 and, for the highest

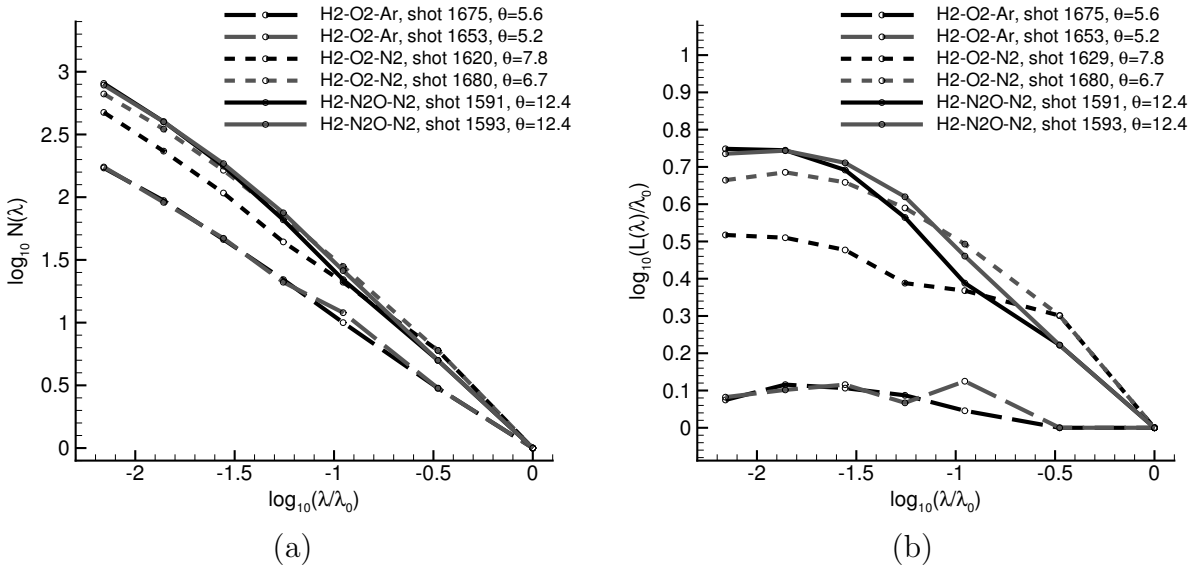

Figure 6: (a) Box-coverage count $N(\lambda)$ as a function of normalized scale for six representative images. (b) Normalized box-coverage length L as a function of normalized scale.

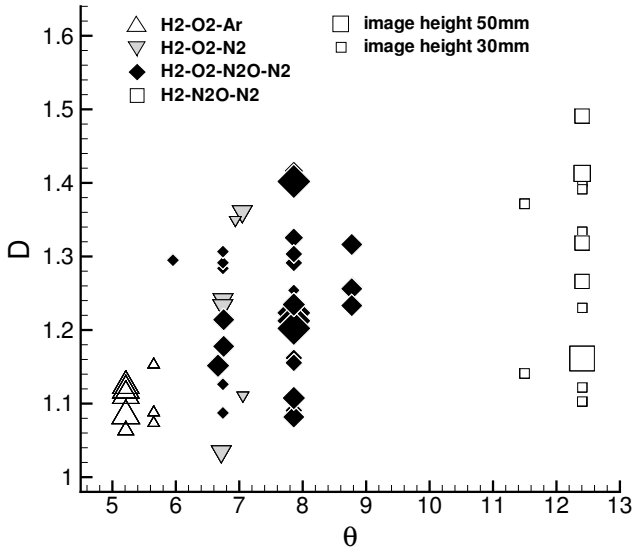

Figure 7: Dimension obtained from least-square linear fit as a function of the reduced activation energy θ. Symbol size scales with height of field of view.

value of $\theta = 12.4$, the maximum dimension of 1.5 is obtained. The larger maximum values of the dimensions obtained for higher values of θ are quantitative evidence for the increasing degree of corrugation of the reaction front for higher values of θ.

Discussion

The large range of dimensions obtained for $\theta > 6$ can be explained, in part, by the same effects that were discussed earlier in connection with the spread of normalized edge lengths shown in Fig. 5.

Additionally, the pixelation of the image and the edge representation affects the box counting method. The box count will vary depending on the edge orientation with respect to the pixel grid. For example, a straight line is represented as a straight line on all scales only if it is inclined to the pixel grid at 45°. When the box size approaches the pixel size, the inferred dimension will decrease toward one, which is expected, since the effective dimension at the pixel scale is one. Analysis of synthetic images of the Koch curve shows a decrease in $d \log L(\lambda)/d \log \lambda$ with decreasing λ, for $\lambda \leq 4$ pixel. With the box counting technique, $d \log L(\lambda)/d \log \lambda$ does not approach zero in a smooth fashion, a consequence of the pixel representation itself. A bounding box partition method (Catrakis and Dimotakis, 1996) based on the idea of representing the boundary outline as B-splines and subsequently subdividing the bounding box in both dimensions in each step, is shown to remove several difficulties based on pixel-based schemes. However, this technique is limited in applicability, since the bounding box in the case of the PLIF images has a high aspect ratio, which leads to a very small tile size close to the resolution limit in the

horizontal direction after a few subdividing steps.

Another reason for the continuous decrease in the slope of $d\log N(\lambda)/d\log\lambda$ with decreasing λ is the steep fall-off in the MTF for low frequencies. The increasing blur for smaller features results in a smoother edge-detected front at smaller scales, and consequently, a decrease in $d\log N(\lambda)/d\log\lambda$ and $d\log L(\lambda)/d\log\lambda$. In addition, one has to consider the light sheet thickness, which reduces the resolvable scale further. We conclude that the decrease in dimension observed for some images of N_2-diluted H_2-O_2 and H_2-N_2O mixtures for scale sizes on the order of 1 mm is most likely not caused by the absence of smaller scale features in the flow, but an effect arising from the box counting technique and the imaging system and technique.

Relevance to Diffusive Transport

For the assumed cut-off scales and fractal dimensions, fractal geometry concepts have been shown to provide estimates of the turbulent flame velocity in combustion research (Gouldin, 1987). The ratio of turbulent burning velocity S_T to laminar burning velocity S_L was first suggested by Damköhler (1940) to be proportional to the ratio of wrinkled flame surface area A_w to the flow cross section area A_0. Here, this concept is applied to investigate the possible contribution of a diffusion-controlled combustion mode to detonation propagation, which, in the classical models, is considered to be due only to shock-induced reaction with no diffusive transport.

The surface area of the reaction front is estimated from the fractal dimension. From the PLIF images, we obtain only a two-dimensional cross section of the three dimensionally corrugated reaction front surface. Assuming fractal isotropy, the fractal dimension D_3 of an object in three dimensions is, due to self-similarity, one greater than the fractal dimension D_2 of a two-dimensional cross section of the same object (Smallwood et al., 1995). The fractal dimensions D_2 obtained from the PLIF images were, at maximum, 1.5, so, for the cases considered, D_3 is, at most, approximately 2.5. In order to compute the three-dimensional surface area from the fractal dimension, the following relationship used in low-speed turbulent combustion research (Gouldin, 1987) has been applied:

$$\frac{A_w}{A_0} = A\left(\frac{\varepsilon_o}{\varepsilon_i}\right)^{D_3-2}, \tag{5}$$

where A is a model constant on the order of one. For a model constant $A = 1$, this leads to a value for A_w/A_0 of 4.8, using for the inner and outer cut-off 4 and 96, respectively. Based on mass conservation considerations, the ratio A_w/A_0 has to be on the order of w/S_L for a diffusion-dominated adiabatic flame to contribute to the combustion, where w is the post-shock velocity in the shock fixed frame, and S_L is the adiabatic flame speed for post-shock conditions. The computation of the adiabatic burning velocity S_L at post-shock conditions was performed with a numerical solution of the one-dimensional steady reactive Navier-Stokes equation with the detailed chemical reaction mechanism as described in Singh et al. (2003). The post-shock conditions were evaluated for a

detonation traveling with $U/U_{CJ} = 0.95$ in a mixture of $2H_2+O_2+8.1N_2$ ($P_0 = 20$ kPa, $T_0 = 300$ K) to be $P_{ps} = 0.39$ MPa and $T_{ps} = 1195$ K. The corresponding adiabatic burning velocity was calculated to be 30.4 m/s. The post-shock velocity is 320 m/s at these conditions, which leads to the criterion of $A_w/A_0 \approx 10.5$ for a diffusive burning process contributing significantly to the combustion mode. This is a factor of two smaller than the surface area increase predicted from the fractal geometry approach. Better resolution of the PLIF images could allow for a smaller inner cut-off ε_i and larger values for A_w/A_0, possibly satisfying the criterion mentioned above.

Conclusions

A quantitative analysis of the OH front geometry of detonations visualized by PLIF imaging has been carried out. Mixtures with various degrees of cellular instability from "regular" to "highly irregular", corresponding to reduced effective activation energies $5.2 \leq \theta \leq 12.4$, have been studied. The geometric complexity of the OH front has been characterized in two ways. First, we have used an approximate integration method to find the total edge length normalized by the image height. Second, we have used the box counting method of fractal analysis to determine an effective dimension of the fronts. Both measures for the geometric complexity correlate well with the effective activation energy θ. For the "regular" mixtures ($\theta \leq 6$), the normalized edge length ranges from 1 to 1.8, small compared to the other mixtures studied. For the "highly irregular" mixtures ($\theta \approx 12.4$), values up to 7.5 are measured. The effective dimension ranges for mixtures with $\theta \leq 6$ up to 1.15 and for mixtures with $\theta \approx 12.4$ up to 1.5. Intermediate values for the normalized edge length and dimension were found for mixtures with intermediate values for θ. The range of scales resolved in the present study were not sufficient to make a definitive conclusion about the possible role of diffusion in the combustion process.

Acknowledgments

This work was supported by Stanford University Contract PY-1905 under Dept. of Navy Grant No. N00014-02-1-0589 "Pulse Detonation Engines: Initiation, Propagation, and Performance".

References

J. Austin. *The Role of Instability in Gaseous Detonation*. PhD thesis, California Institute of Technology, Pasadena, California, June 2003.

H.J. Catrakis and P.E. Dimotakis. Mixing in turbulent jets: scalar measures and isosurface geometry. *Journal of Fluid Mechanics*, 317:369–406, 1996.

N. T. Clemens. Flow imaging. In J. P. Hornak, editor, *Encyclopedia of Imaging Science and Technology*, pages 390–420. John Wiley and Sons, New York, 2002.

G. Damköhler. Der Einfluss der Turbulenz auf die Flammengeschwindigkeit in Gasgemischen. *Zeitschrift für Elektrochemie*, 46(11):601–652, 1940.

F. Gouldin. An application of fractals to modeling premixed turbulent flames. *Combustion and Flame*, 68:249–266, 1987.

R.J. Kee, F.M. Rupley, and J.A. Miller. CHEMKIN-II: A FORTRAN chemical kinetics package for the analysis of gas-phase chemical kinetics. Technical Report SAND89-8009, Sandia National Laboratory, 1989.

J.C. Libouton, A. Jacques, and P.J. Van Tiggelen. Cinétique, structure et entretien des ondes de détonation. *Actes du Colloque International Berthelot-Vieille-Mallard-Le Chatelier*, 2:437–442, 1981. Bordeaux.

M.A. Mueller, R.A. Yetter, and F.L. Dryer. Kinetic modeling of the $CO/H_2O/O_2/NO/SO_2$ system: Implications for high-pressure fall-off in the SO_2+O(+M)=SO_3(+M) reaction. *Int. J. Chem. Kinetics*, 32(6):317–339, 2000.

F. Pintgen. *Laser-Optical Visualization of Detonation Structures.* Diplomarbeit, Lehrstuhl für Thermodynamik: Technische Universität München / Graduate Aeronautical Laboratories: California Institute of Technology, Munich, Germany, December 2000.

F. Pintgen. *Detonation Diffraction in Mixtures with Various Degrees of Regularity.* PhD thesis, California Institute of Technology, December 2004.

F. Pintgen, J. Austin, and J.E. Shepherd. Detonation front structure: Variety and characterization. In G.D. Roy, S.M. Frolov, R.J. Santoro, and S.A. Tsyganov, editors, *Confined Detonations and Pulse Detonation Engines*, pages 105–116. Torus Press, Moscow, 2003a.

F. Pintgen, C.A. Eckett, J. Austin, and J.E. Shepherd. Direct observations of reaction zone structure in propagating detonations. *Combustion and Flame*, 133(3):211–229, 2003b.

J.E. Shepherd. The chemical kinetics of hydrogen-air-diluent detonations. *Prog. Astronaut. Aeronaut.*, 106:263–293, 1986.

S. Singh, D. Lieberman, and J. E. Shepherd. Combustion behind shock waves. Paper 03F-29 Western States Section/Combustion Institute, October 2003.

G.J. Smallwood, Ö.L. Gülder, D.R. Snelling, B.M. Deschamps, and I. Gökalp. Characterization of flame front surfaces in turbulent premixed methane/air combustion. *Combustion and Flame*, 101:461–470, 1995.